

Melt Pond Mapping With High-Resolution SAR: The First View

In this paper, VHR SAR images are successfully used to map melt ponds in the Arctic region, which potentially leads to more accurate estimation of overall energy and mass balance in rapid changing Arctic environment.

By DUK-JIN KIM, Member IEEE, BYONGJUN HWANG, KYUNG HO CHUNG, SANG HOON LEE, HYUNG-SUP JUNG, Member IEEE, AND WOUIL M. MOON, Fellow IEEE

ABSTRACT | Melt pond statistics (size and shape) have previously been retrieved from aerial photography and high-resolution visible satellite data. These submeter- or meter-resolution visible data can provide reasonably accurate information on melt ponds, but are greatly constrained by the limited solar illumination and frequent cloud cover in the Arctic region. In this study, we venture into exploring high-resolution synthetic aperture radar (SAR) or imaging radar method for melt pond mapping, which is not severely disrupted by cloud or low solar zenith angle. We analyzed high-resolution airborne SAR images (0.3-m resolution) of midsummer sea ice, acquired from a helicopter-borne SAR system in the northern Chukchi Sea. The pond area and shape (circularity) derived from the airborne SAR images showed that the statistics were

comparable to those previously observed from aerial photographs. We argue that high-resolution SAR, together with one-to-one comparison with coincident aerial photographs, can be used to map melt ponds at a level of detail comparable to aerial photography or high-resolution optical satellite remote sensing. Our encouraging results suggest the possibility of using high-resolution SAR (current or future systems) to map melt ponds in the Arctic region.

KEYWORDS | Future synthetic aperture radar (SAR) system; high-resolution SAR; melt pond; sea ice

I. INTRODUCTION

Melt ponds are pervasive features of summer Arctic sea ice, and can cover up to 50% of the surface of an ice floe [1]. Melt ponds have a surface albedo four times smaller than snow-covered sea ice [2], and absorb solar light four times more efficiently [3]. Such contrasts make melt ponds have significant influence on surface energy balance [4], ice thickness distribution [5], [6], ice strength [7], and ice-albedo feedback [8]. Sea ice melting can be amplified depending on melt pond fractional coverage, number density, and dimensions (size, depth, and shape), i.e., bigger and wide coverage of melt ponds would enhance absorption by solar energy, weaken ice strength, and increase ice melt. Thus, reliable retrieval of those pond variables by airborne or space-borne sensors is very important in order to improve our understanding and related parameterizations of climate models [5], especially because melt ponds are still poorly represented in climate models.

Current technologies to observe melt pond properties include *in situ* field observation [9], [10], aerial

Manuscript received January 31, 2012; revised July 24, 2012; accepted October 9, 2012. Date of publication January 9, 2013; date of current version February 14, 2013. This work was supported in part by the Space Core Technology Development program through the National Research Foundation of Korea funded by the Ministry of Education, Science and Technology (2011-0020884); in part by the Korea Polar Research Institute under Project PE11040; in part through the ACCESS program, a European Project supported within the Ocean of Tomorrow call of the European Commission 7th Framework Programme; as well as in part by the U.K. Natural Environment Research Council Oceans2025 strategic marine research program. The Royal Society (U.K.) supported the travel costs between the United Kingdom and Korea via the international joint project (JP090400) which helped to build collaborative fieldwork for this study.

D.-J. Kim is with the School of Earth and Environmental Sciences, Seoul National University, Seoul 151-742, Korea.

B. Hwang is with the Scottish Association for Marine Science, Oban, PA37 1QA Argyll, U.K. (e-mail: phil.hwang@sams.ac.uk).

K. H. Chung and **S. H. Lee** are with the Korea Polar Research Institute (KOPRI), Incheon 406-840, Korea.

H.-S. Jung is with the Department of Geo-Informatics, University of Seoul, Seoul 130-743, Korea.

W. M. Moon is with Satellite Geophysics, Faculty of Environment, Earth and Resources, University of Manitoba, Winnipeg, MB R3T 2N2 Canada and also the Research Institute of Oceanography (RIO), School of Earth and Environmental Studies, Seoul National University, Seoul 151 742, Korea.

Digital Object Identifier: 10.1109/JPROC.2012.2226411

photography [11], and visible optical satellite data [12]. *In situ* observation can provide the most accurate, precise measurements of melt pond properties and is indispensable for detailed investigation of physical processes, but this method is very costly and restricted by logistical and accessibility limitations. More extensive mapping of melt pond coverage (ideally at a pan-Arctic scale) is necessary to constrain various climate model parameters. Such large-scale areal observations can only be achieved by aerial survey or/and satellite remote sensing. Aerial survey photography often uses unpiloted aerial vehicles (UAVs) [13] or ship-based helicopters [14], which can provide submeter resolution images and pond fractions at sufficient accuracy to verify the values obtained from moderate resolution imaging spectroradiometer (MODIS) images [13]. Aerial surveys are, however, greatly limited by regional weather and logistics. The MODIS-based method has shown reasonable potential in measuring melt pond fraction and in estimating surface albedo [12], but it cannot derive detailed pond statistics, i.e., size and shape, due to its moderate resolution. Such detailed pond statistics (including pond fraction) can be derived from high-resolution (1-m resolution) visible optical satellite images [15]. However, pervasive cloud coverage during the Arctic summer (about 80%) hinders melt pond mapping via any visible optical sensor-based methods [16].

Satellite synthetic aperture radar (SAR) offers undisturbed observation of sea ice regardless of cloud coverage or darkness. Conventional SAR data (e.g., ENVISAT ASAR and Radarsat-1) offer a spatial resolution of the order of tens to hundreds of meters. Such SAR data have shown some potential for monitoring general melt processes (e.g., onset of melt, surface albedo) [17], [18]. However, we are not aware of any previous studies that fully explored the potential of SAR data in mapping melt ponds; this may have been due to the spatial resolution and speckle noise of such SAR data. However, present-day high-resolution SAR sensors (e.g., TerraSAR-X, COSMO-SkyMed, and Radarsat-2) can achieve up to 1-m spatial resolution and submeter resolution will be realized in future SAR missions (e.g., TerraSAR-X2) [19].

This raises the question of whether it is possible to map melt ponds using current or future high-resolution SAR systems. If so, what kinds of pond statistics can be derived and at what level of detail? To address these questions, we conducted a helicopter-based airborne SAR survey in the northern Chukchi Sea during summer 2011. The airborne SAR system successfully mapped sea ice at 0.3-m resolution along with coincident TerraSAR-X (StripMap dual polarization, 6-m resolution) data acquisition. This allowed us to derive fraction, size, and shape data for melt ponds as small as approximately 10 m². We report on the first known attempt to map melt ponds in detail within the context of potential applications of future space-borne high-resolution SAR systems.

II. BACKGROUND

A. Seasonal Evolution of Melt Ponds

With increasing solar radiation in spring, excessive solar energy initially causes melting of snow and the upper surface of sea ice [20]. Storm events sometimes accelerate snow melt, and thus, the formation of melt ponds [21]. Melt water gravitates to lower surfaces, on which pools of water start to collect (Fig. 1). On first-year ice, surface topography is affected mostly by snow accumulation and windblown snow drift [22], while on multiyear ice, melt ponds form in depressions remaining from previous years. At this stage, ice permeability is low and sea ice temperature is below the melting point [23]. This prevents drainage of melt water except through cracks or flaws. Early melt ponds on first-year ice are mostly wide and shallow and their perimeters are irregular and complex [24]. As melting progresses into summer, the ice permeability increases (by two orders of magnitude) [23] and melting increases at the bottom and lateral edges of the ponds. The ponds start to form a distinct shape, vertical drainage becomes much faster, and ponds become deeper and connect to the underlying seawater, forming “through” dark-looking melt ponds. The ponds are often interconnected, forming large and complex networks [24] (Fig. 1). Finally, the pond area fraction diminishes as ice floes melt out and break up, and melt ponds start to freeze up and snow begins to accumulate on the frozen melt ponds (Fig. 1).

Melt pond properties differ between first-year and multiyear ice. First-year ice has a greater variability in pond area fraction than multiyear ice. A pond area fraction of 0.3–0.8 was typically observed on first-year ice floes [1], [7], [25], [26], although in some cases, no melt ponds were observed on first-year ice floes [24]. In the case of multiyear ice floes, a pond area fraction of 0.2–0.3 was typically observed [1], [11], [27]. Melt ponds on multiyear ice tend to be deeper (about 60 cm) than those on first-year ice (about 40 cm) [25].

B. Current Remote Sensing Techniques for Melt Pond Mapping

Current remote sensing methods for melt pond mapping can be categorized as either airborne or space-borne methods. Airborne methods include aerial photography (digital camera or video system), sometimes onboard a helicopter stationed on a ship or ice camp (e.g., [24]) or using long-range manned as well as unpiloted aircraft [11], [13]. Such observations typically provide submeter image resolution. Being of such high resolution, melt pond fractions and statistics retrieved from aerial photographs can provide more accurate data than present-day satellite-derived results. Continuous helicopter-based observation at the Surface Heat Budget of the Arctic Ocean (SHEBA) ice camp has provided invaluable information on the seasonal evolution of melt ponds near the drifting ice camp

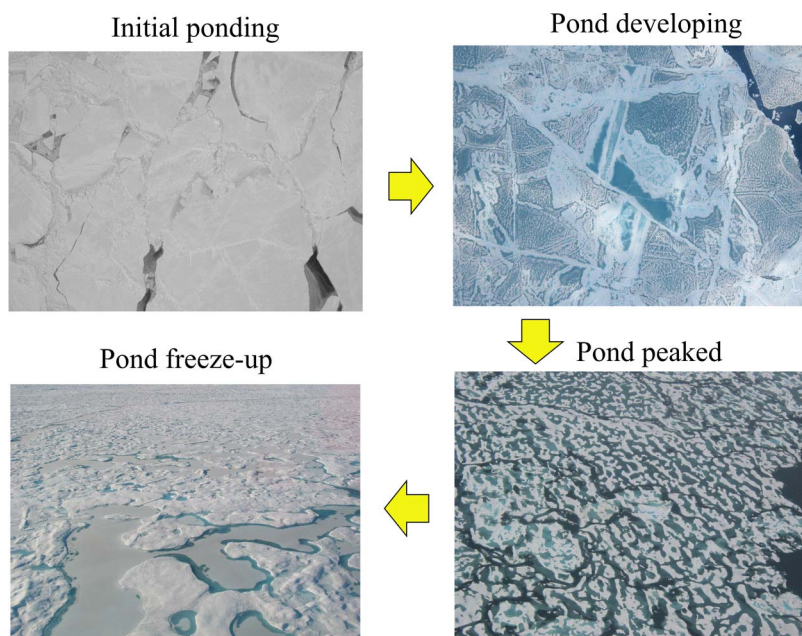


Fig. 1. Photographic views of melt ponds at different stages of their evolution. (Photographs correspond to various locations in the Arctic.)

site [24]. Long-range aircraft observations were often used as the validation data set for satellite-derived melt pond mapping [13] or to take snapshots of surface features at specific times [11].

To date, space-borne observations mostly use visible-spectrum bandwidths with medium-resolution sensors (e.g., MODIS [12]) or high-resolution sensors (e.g., IKONOS [15]). The broader swath of medium-resolution satellite images can provide wider coverage of pond fraction and aggregated surface albedo estimates. MODIS-derived melt pond fraction and surface albedo are generally consistent with UAV-derived values [13]. Cloud cover usually becomes more persistent later in the melting season, when the melt pond fractions typically reach their peaks [13], [24]. This makes it difficult to derive melt pond properties when they are most needed. However, frequent coverage of MODIS in the Arctic may reduce the data gap caused by persistent cloud cover. Landsat 7 ETM+ images have also been used to derive melt pond fraction [28], [29]. Such images have much higher spatial resolution (approximately 30 m) than MODIS (250 m) and could provide more accurate melt pond fractions. However, there are fewer usable scenes, due to the longer revisit time of 16 days and persistent cloud cover over the Arctic. In addition, images tend to be saturated in summer when sun elevation is high [12].

C. Need for High-Resolution SAR

It is clear that the MODIS-based method appears to provide the most useful melt pond data at wider coverage than other satellite-based methods. However, it cannot

provide detailed pond statistics of area and shape, due to its moderate image resolution (maximum of 250 m in visible bands). Statistical characteristics of pond size and shape are required in order to apply constraints on climate model parameters and better understand the evolution and radiative properties of melt ponds [3], [30]. Such pond statistics have been retrieved from aerial photographs [24] or from high-resolution visible satellite images [15]. In the former case, the statistics were obtained from 12 survey flights at SHEBA site during the spring/summer of 1998, and thus the retrieved statistics cover one summer at one drifting site. Fetterer *et al.* [15] took a different approach by using high-resolution (1-m resolution) satellite imagery. They obtained pond statistics within 500-m² cells at four fixed sites across the Arctic Ocean, and thus the retrieved statistics would be more representative of the wider Arctic Ocean. The images are often separated by a week or more due to cloud cover and longer revisit time, and so is the retrieval of pond statistics [15]. Even at such irregular temporal resolution, one can capture major sea ice events, but it is still difficult to obtain pond fraction and statistics at the location and time that we need. The practical alternative for reliable retrieval of pond fraction and statistics at any required time and location is to use a space-borne SAR system. Such capability with space-borne SAR is critical, as the pond fraction can change significantly within a few days [24]. Some current high-resolution satellite-borne SAR systems offer up to 1-m resolution and flexibility for scientific users to order future scenes at specified times, allowing researchers to derive melt pond statistics at any

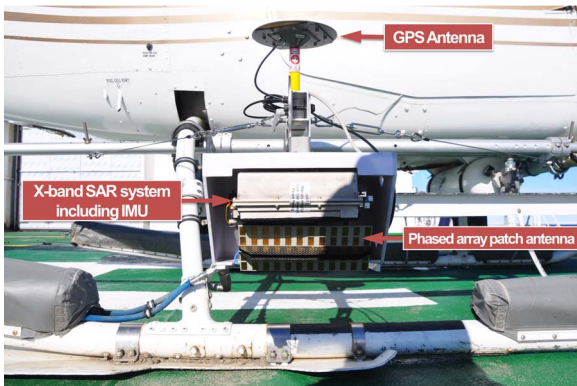


Fig. 2. A photograph of the airborne SAR system.

time. However, no attempt has yet been made to extract melt pond statistics from high-resolution SAR data; this paper discusses some of our attempts to evaluate helicopter-borne and satellite-borne SAR data to estimate melt pond statistics.

III. HELICOPTER-BORNE SAR AND SPACE-BORNE SAR MEASUREMENTS

To test the feasibility of using high-resolution SAR for melt pond mapping, a helicopter-based airborne SAR survey was conducted as a part of the 2011 KOPRI-led *R/V Araon* Arctic scientific cruise. An X-band SAR (NanoSAR) unit was mounted on a helicopter (Bell 206 Jet Ranger) stationed on *R/V Araon*. A laptop computer in the cabin connected to the unit through a RJ-45 Ethernet cable was used to control and log data (Fig. 2). The NanoSAR system was equipped with Global Positioning System/inertial measurement units (GPS/IMUs) and a gimbal-mounted phased array antenna in order to compensate for the motion of the helicopter. The relevant technical parameters of the NanoSAR system are summarized in Table 1. The maximum resolution can be set to 0.3 m and the image swath can be variable between 0.5 and 4 km depending on flight altitude and resolution setting. In our experiment, we set the maximum resolution of 0.3 m for the survey at a flight altitude of 300 m.

Table 1 Basic System Parameters of Airborne SAR

Parameters	Description
Transmit frequency	10.25 GHz (X-band)
Transmit power	1 Watts
Bandwidth	500 MHz
Resolution	0.3, 0.5, 1, 2, and 5 m
Polarization	HH
Swath width	0.5 to 4 km

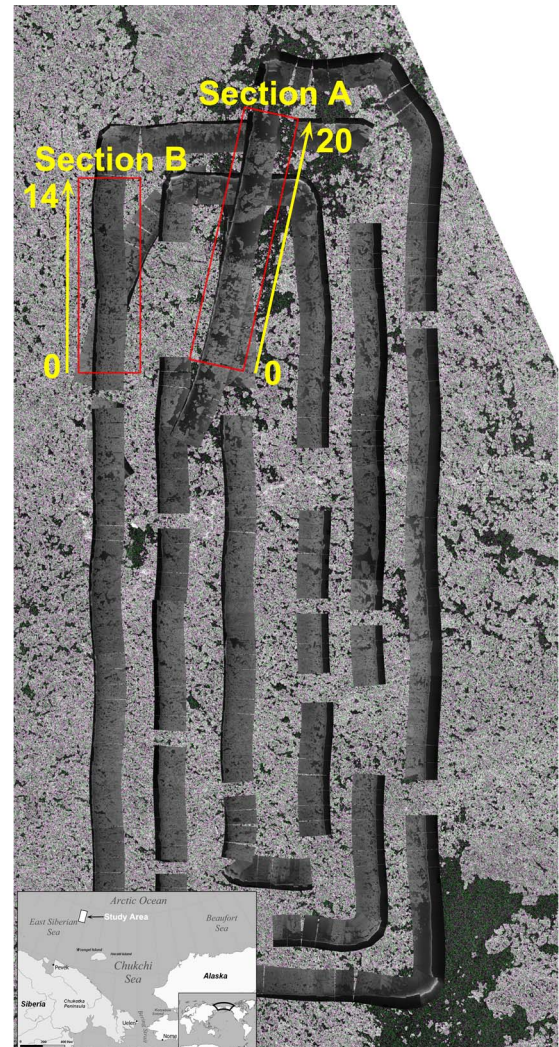


Fig. 3. The mosaic of airborne SAR images overlaid on the top of a TerraSAR-X SM image. The geographic location of the survey area is shown as the white box in the map on the bottom left. Sections A and B (red boxes) mark the location of the selected airborne SAR images, and the number (yellow) indicates the image number shown in Fig. 6.

The airborne SAR survey started from the ship at 04:48 coordinated universal time (UTC) on August 12, 2011, and continued for 1 h. The geographic location of the survey region is in northern Chukchi Sea, as shown in Fig. 3. The sea ice condition in the area mainly comprises small (about 100 m in size), heavily melted ice floes that hold no melt ponds on the surface (Fig. 4). Thicker and larger multiyear ice floes among the small thinner floes hold melt ponds on the surface; some ponds are blue while others appear dark, and some melt ponds were refrozen on the surface. Coincident with the helicopter survey, we acquired a TerraSAR-X Stripmap mode (SM) image (6-m resolution and dual (HH and VV) polarization) at 04:55 UTC covering the entire survey area (Fig. 3).

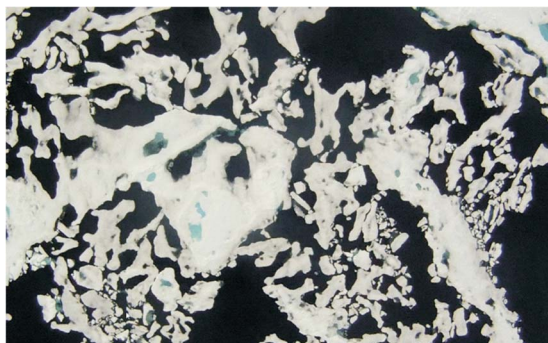


Fig. 4. An aerial view of the sea ice condition in the survey area. Large multiyear ice floes with blue melt ponds are visible in small broken, heavily melted ice floes.

IV. MELT POND MAPPING FROM HIGH-RESOLUTION SAR

A. Melt Pond Mapping Procedure

We took the following steps to obtain melt pond fraction and statistics from airborne SAR images. We first delineate the ice and melt pond features using image processing software (ENVI[®] EX), based on the combination of multiscale segmentation and aggregation methods [31]. An example is shown in Fig. 5, in which red-colored polygons are the delineated melt pond features while blue-colored polygons represent ice. Here, we define any polygons within the ice polygon as melt ponds. During the feature extraction procedure, we used the same scale and aggregation factors for all of the images. The feature-extracted image was then exported as a binarized image of water and ice, which was then processed to detect melt ponds and calculate pond fraction, number density, area, and perimeter length. Ice and pond parameters used in this paper were defined following Perovich *et al.* [24]. The fraction of ice (A_i) is the area fraction of the ice (excluding pond area) within the image, and the fraction of pond (A_p) is the area fraction of ponds within the image. The fraction of the ice that is ponded (A_p^*) is defined as $A_p^* = A_p / (A_i + A_p)$, which adjusts the pond fraction to account for variable sea ice concentration. For pond statistics, we calculate number density (N_d), pond area (S_p), and circularity (C_p). N_d is defined as the number of ponds per the area of ice and ponds ($A_i + A_p$) (in square kilometers). Pond size (S_p) is defined as the polygon area occupied by a pond (in square meters). The circularity of pond (C_p) is defined as $C_p = P^2 / S_p$, where P is the perimeter.

A total of 36 airborne SAR images were selected in this study to investigate the feasibility of using high-resolution SAR data for the melt pond mapping. The images were obtained from two sections of airborne SAR flight strip, as shown in Fig. 3. Due to technical problems, the obtained SAR images could not be combined into a perfectly continuous strip image. The original image resolution (0.3 m)

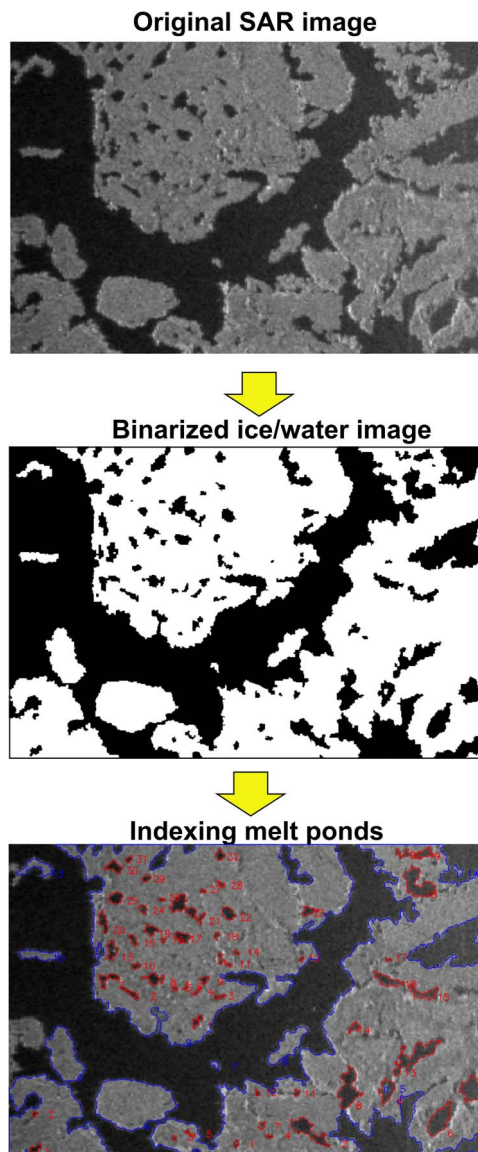


Fig. 5. The melt pond mapping procedure. Ice/water binarized image is first obtained from the original airborne SAR image using ENVI[®] EX (multiscale feature extraction). From the binarized image, melt ponds are detected by identifying water polygons enclosed within the ice polygon. In the binarized image, white color indicates ice pixels while black color indicates water/pond pixels. Melt ponds are then indexed and numbered in red, and ice floes are indexed and numbered in blue.

was degraded to 0.6 m while converting SAR complex data into the amplitude image in order to reduce speckle noise. Thus, each SAR image has a size of approximately 600 m (range) by 350 m (azimuth) with 0.6-m pixel size. The near-range part of SAR images sometimes has dark image tone due to no backscattered signal in a predetermined time domain, so we cropped out the edges before the analysis, leaving a final SAR image of approximately 500 m (range) by 350 m (azimuth). For each image, we

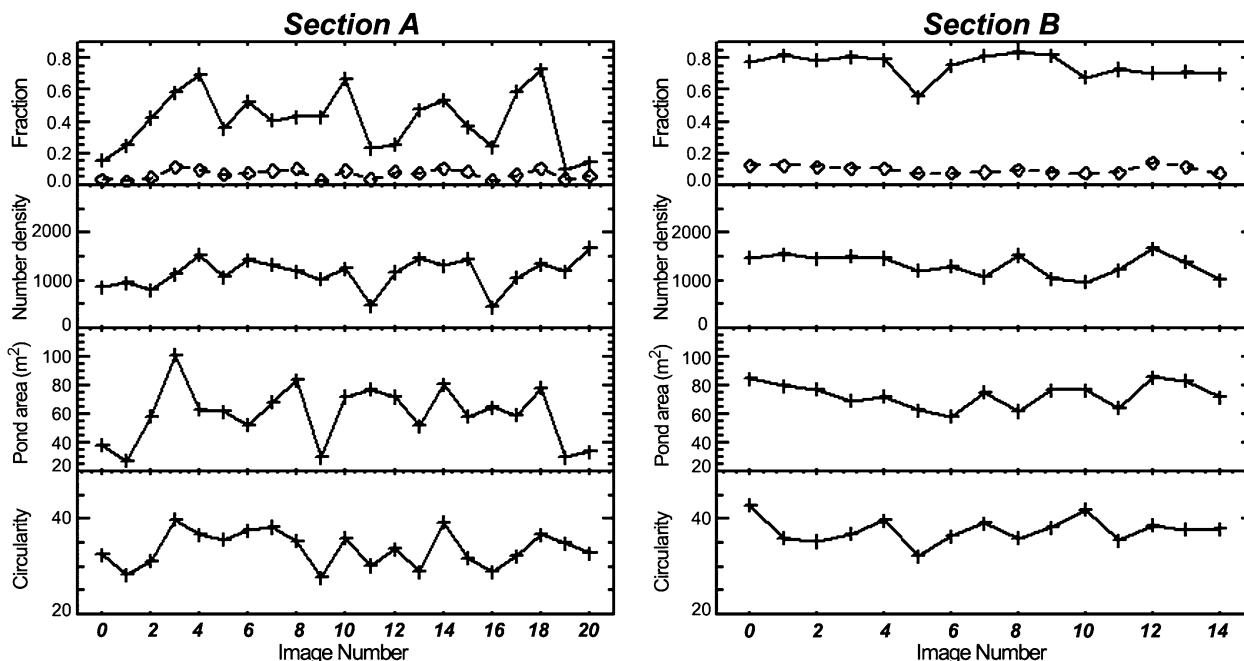


Fig. 6. Fractional coverage of ice (A_i) and melt pond (A_p^*), number density (N_d), pond size (S_p), and circularity (C_p) are plotted with respect to the image number in sections A and B. In the top panel, the solid line with plus symbols represents A_i and the dashed line with open diamond symbols represents A_p^* . Image numbers are shown in Fig. 3.

derived A_i , A_p , A_p^* , and N_d , as described above. The pond area was calculated as an area confined by pond polygon (i.e., polygon area) not calculated as a pixel area, and perimeter was calculated as the total length of the polygon boundary. All pond polygons with less than 25 pixels were excluded from the analysis because such small ponds were difficult to be derived consistently. Note that the minimum pond area can be smaller than 9 m², because we used

polygon area. All ponds with an area larger than 700 m² were also excluded from the analysis because, in some images, the open water area within interconnected ice floes can be mistakenly classified as melt ponds. These open water areas are generally much larger than ponds, so setting a maximum pond area can remove those potentially misclassified areas of open water. This type of filtering can also remove some “real” large melt ponds. However, the

Table 2 Overall Pond Fraction and Statistics Derived From the Airborne SAR and TerraSAR-X SM Images Within Section A

System	Pond statistics	A_i	A_p^*	N_d	S_p	C_p
Airborne SAR	Mean	0.41	0.07	1148	66.2	35.1
	Standard Deviation	0.19	0.03	320	89.5	20.7
	Min.	0.10	0.03	439	5.4	14.3
	Max.	0.73	0.11	1678	670.5	211.7
TerraSAR-X SM		0.58	0.02	n/a	n/a	n/a

Table 3 Overall Pond Fraction and Statistics Derived From the Airborne SAR and TerraSAR-X SM Images Within Section B

System	Pond statistics	A_i	A_p^*	N_d	S_p	C_p
Airborne SAR	Mean	0.75	0.10	1326	73.9	37.6
	Standard Deviation	0.07	0.02	224	101.1	22.8
	Min.	0.56	0.07	964	5.4	14.9
	Max.	0.88	0.14	1671	697.7	206.9
TerraSAR-X SM		0.94	0.02	n/a	n/a	n/a

actual number density of such large ponds is very small (less than 4%).

B. Melt Pond Fraction and Statistics

The variability of pond parameters for two selected regions (sections A and B) is shown in Fig. 6, and the overall statistics are listed in Tables 2 and 3. Both cases represent a wide range of sea ice conditions, from almost open water ($A_i = 0.1$) to almost 88% ice cover. Recall that the SAR image size used for the analysis is about $500 \text{ m} \times 350 \text{ m}$. Large open water areas or ice fractions are thus simply attributed to the presence of open water patches or large ice floes, respectively, within the image's field of view. Contrasting ice conditions between sections A and B can be clearly seen in the TerraSAR-X SM image, acquired during the same period as the airborne SAR survey (Fig. 7). This contrasting condition can also be seen in the much lower ice fraction within section A than in section B (Tables 2 and 3).

The pond fraction (A_p^*) also shows the difference between sections A and B (Tables 2 and 3). The slightly higher pond fraction in section B can be attributed to a larger fraction of multiyear ice floes in that region. The mean pond fractions in both regions are smaller than typical values (0.2–0.3) observed on summer multiyear ice (e.g., [13] and [24]). The mean number density N_d of the detected ponds is only between 1148 and 1326 km^{-2} , which is much smaller than the numbers observed during SHEBA [24]. While our data show smaller pond fraction

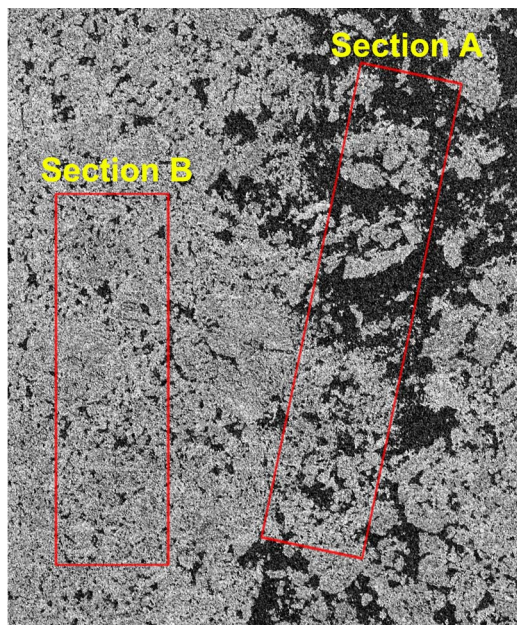


Fig. 7. The TerraSAR-X SM image (HH polarization) acquired coincidentally with the airborne SAR survey. The two red boxes mark the geographical boundary of sections A and B of the airborne SAR images analyzed in this research.

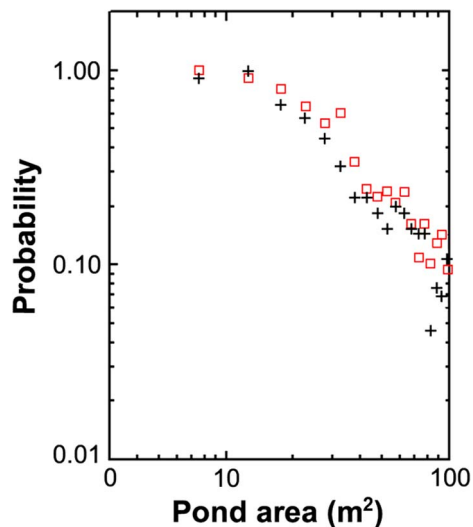


Fig. 8. Distribution of pond size (area) (S_p). Black crosses and red diamonds represent values in sections A and B, respectively. Both x - and y -axes of the plot are scaled logarithmically.

and number density, our values for the pond area and circularity are comparable to the SHEBA observations. Our data show a mean pond size of 66.2–73.9 m^2 (Tables 2 and 3). These values are quite comparable or slightly larger than the pond sizes observed on August 7, 2011, at the SHEBA site [24]. In the SHEBA case, the observed pond circularity was 38.5–41.2 [24]. For comparison, mean values were 35.1–37.6 (Tables 2 and 3) in this case. These comparable results indicate that melt ponds on thicker multiyear ice floes would have similar size and shape as those observed during SHEBA. On the other hand, the smaller pond fraction and number density can be attributed to a large fraction of small, melted ice floes without melt ponds, as seen in Fig. 4.

Following Perovich *et al.* [24], the pond size (area) distribution can be fitted by a power law, $y = aX^b$. In their case, the size distribution was well fitted with an exponent b of -1.5 and the correlation coefficient of more than 0.99. In our case, for sections A and B, the pond size distribution shows similar linear decrease in logarithm scale (Fig. 8). Flattening of the distribution is visible in the range less than 10 m^2 , indicating inability to accurately detect ponds smaller than 10 m^2 . The fitting was, therefore, made within the range $10\text{--}100 \text{ m}^2$, and the b exponents of -1.3 and -1.2 were estimated with correlation coefficients of 0.95 and 0.96 for sections A and B, respectively.

C. Comparison With the Aerial Photograph

While our pond statistics of area and shape are comparable to the previously reported values from aerial photographs, the question still remains: how well do they match each other in detecting melt ponds? To answer this question, an example of one-to-one comparison between

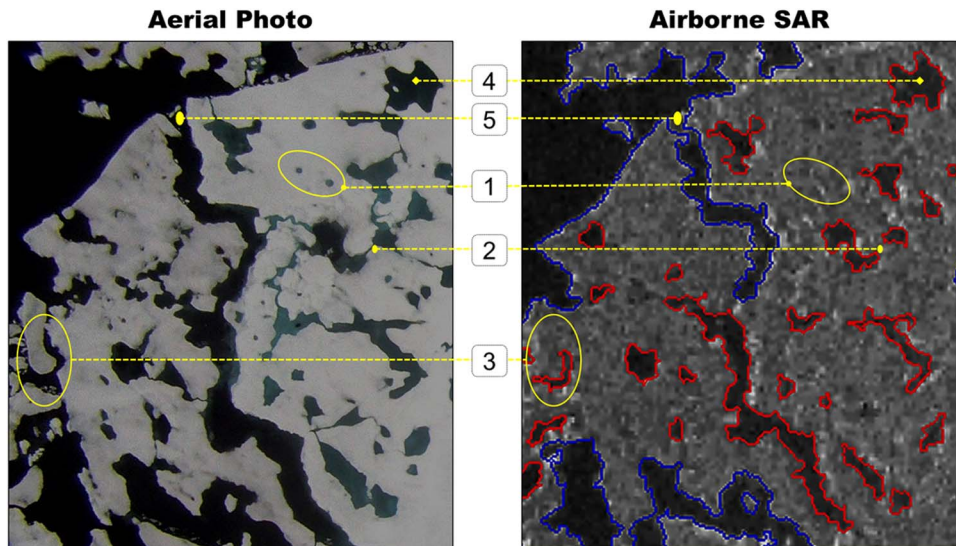


Fig. 9. Comparison between the aerial photograph and the airborne SAR images. Notice that the aerial photograph is highly distorted, and hence, the sizes of melt ponds in the aerial photograph cannot be directly compared with those in the airborne SAR image acquired in this study.

the aerial photograph and the airborne SAR images was investigated (Fig. 9). The comparison shows that most small melt ponds seen in the aerial photograph are not detected in the airborne SAR image (see number 1 in Fig. 9, for example). This is what we expect because we set the minimum number of 25 pixels as the lowest limit or they are simply too small to be detected from the airborne SAR image. The aerial photograph shows that melt ponds are interconnected by small channels. However, these small channels are not detected in the airborne SAR images (see number 2 in Fig. 9). This may affect the pond circularity estimates from the airborne SAR image, but the pond area estimates would not be significantly affected. Recall that the maximum area for melt pond detection was set to 700 m^2 in order to reduce the number of open water areas surrounded by attached ice floes that would be misclassified as melt ponds. This does effectively reduce the false-positive classification of melt ponds in the case of larger areas with open water, but some small areas of open water can still be misrepresented as melt ponds (see number 3 in Fig. 9). A floe-separation algorithm (e.g., erosion and expansion filter) could be used to reduce the chance of detecting such false melt ponds. Although these problems described above have not been eliminated in the SAR method, the shape and size of melt ponds derived in the image closely resemble those shown in the aerial photograph (see number 4 in Fig. 9). In addition, some of the larger channels can be clearly detected even from the SAR image (see number 5 in Fig. 9). Note that the aerial photograph is geometrically distorted, so a direct quantitative comparison between the aerial photograph and the airborne SAR images is difficult. However, the polygon

boundaries of the ponds detected in the airborne SAR image clearly define the same ponds visible in aerial photographs, even for melt ponds with very complex shapes. This suggests that the shape and the size of ponds can be detected in as much detail using SAR as from the aerial photographs.

D. Comparison With the TerraSAR-X SM Image

In this section, we compare melt pond mapping between airborne SAR and TerraSAR-X SM images. The acquired TerraSAR-X SM data were radiometrically calibrated and resampled to 3-m resolution. Note that TerraSAR-X can offer up to 1-m resolution in the high-resolution spotlight (HRS) mode. It was not possible to synchronize the acquisition of the TerraSAR-X HRS image with the airborne SAR survey, due to the unpredictability of the ship's cruise schedule, weather conditions, and the small swath width of the HRS mode. For the melt pond mapping from TerraSAR-X SM images, we employed the same procedure as for airborne SAR data analyses; all ponds with less than 25 pixels or larger than 700 m^2 in the area were excluded from the analysis. Fig. 10 shows an example of the one-to-one comparison of melt pond detection between airborne SAR and TerraSAR-X SM images. It clearly demonstrates the failure of detecting small melt ponds in the TerraSAR-X image (see number 1 in Fig. 10). In this case, the maximum pond area is 128.5 m^2 . This limitation can be clearly seen in the pond fraction (A_p^*) (Tables 2 and 3), in which the TerraSAR-X SM significantly underestimates the pond fraction compared to the airborne results.

Subarea 2 in Fig. 10 shows large melt ponds detected in the TerraSAR-X SM image. The pond areas estimated

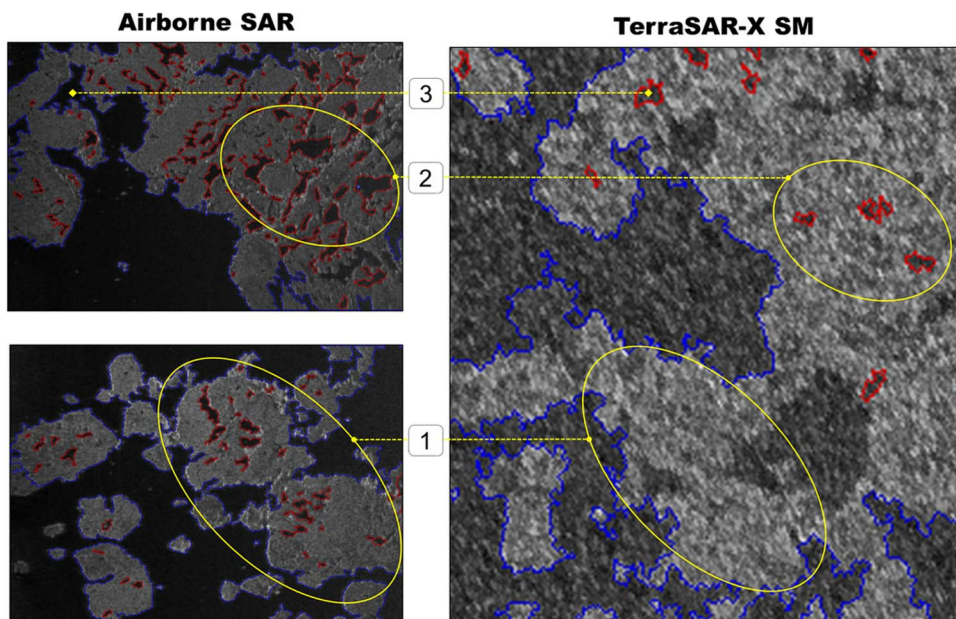


Fig. 10. Comparison of melt pond mapping between airborne SAR (left) and TerraSAR-X SM (right) images.

from the TerraSAR-X SM image range approximately from 237.5 to 543.8 m². These pond area estimates are about 20%–40% smaller than those observed from the airborne SAR images (i.e., 367.0–670.5 m²). The smaller pond areas estimated from the TerraSAR-X SM image are likely due to blurring by the coarser spatial resolution. Subarea 3 shows the case of detecting open water areas as melt ponds. Due to the coarser resolution of the TerraSAR-X SM image, TerraSAR-X SM melt-pond mapping is more severely affected by this caveat, i.e., the open water area surrounded by attached ice floes is subject to misclassification as melt ponds. Removing ponds with an area larger than 700 m² can reduce such classification errors to some extent, but small areas of open water can still be incorrectly classified as melt ponds.

V. DISCUSSION AND CONCLUSION

Previously, detailed melt pond statistics have usually been derived from aerial photographs or high-resolution visible satellite data. These types of meter or submeter resolutions provide quite accurate information on melt ponds, but data acquisition in the Arctic is greatly constrained by logistical challenges and weather, including frequent cloud cover. In this study, we explored a high-resolution SAR method for the melt pond mapping, which is not affected by cloud coverage or limited solar illumination. During summer 2011, we acquired high-resolution (0.3-m resolution) SAR data over summer sea ice in the northern Chukchi Sea, using a helicopter-mounted X-band airborne SAR system (NanoSAR). The acquired high-resolution SAR images were processed using a combination of a multiscale feature

extraction algorithm (ENVI[®] EX) and a IDL[®] codes that automatically index and derive pond statistics of the classified image from the feature extraction algorithm.

A total of 36 airborne SAR images were analyzed to estimate and derive pond fraction and pond statistics of the area and shape (circularity). Our results show that the pond fraction and the number density derived from the airborne SAR images are smaller than the previously observed information from aerial photographs, yet the pond area and circularity are comparable to previous observations. The smaller fraction and number density of ponds can be attributed to the large fraction of small, melted ice floes without melt ponds contained within the survey area. At the same time, the close agreements of the pond area and circularity results indicate that melt ponds on large and thick multiyear ice floes would be statistically similar to those observed during the SHEBA experiment. The above results are supported by the fact that the pond size (area) distributions from airborne SAR images are well fitted by a power law with the exponent values that are comparable to the previous SHEBA observation.

A one-to-one comparison with an aerial survey photograph demonstrated both successes and caveats of melt pond mapping with airborne high-resolution SAR data. The comparison showed that SAR data, even at submeter resolution, is more prone to misclassify the areas of open water within interconnected ice floes as being melt ponds. Despite this caveat, the shape and the size of melt ponds shown in airborne SAR images appear quite similar to those seen in aerial photographs. The results of this study indicate that the size and the shape of melt ponds derived from the high-resolution SAR could provide a level of

detail and accuracy comparable to that obtained from aerial photographs.

Comparison with the TerraSAR-X SM image shows clear failure of TerraSAR-X SM data in detecting small melt ponds (e.g., less than 130 m²). Some large melt ponds (larger than 367 m²) can easily be detected in the TerraSAR-X SM image, but the estimated areas of the detected ponds are smaller than those observed from the airborne SAR image, which appear more similar to ground-truth observations. The TerraSAR-X SM image also significantly underestimates the pond fraction, compared to the airborne SAR results.

The results of this study are very encouraging, in that detailed melt pond mapping can be achieved using a high-resolution (down to 0.3-m resolution) SAR system.

Although determination of the feasibility of melt pond mapping with space-borne SAR data still requires further investigation, this study has clearly demonstrated that space-borne high-resolution SAR systems, if spatial resolution is sufficiently high enough, could be effectively and economically utilized in melt pond mapping in Arctic areas. ■

Acknowledgment

The authors would like to thank *R/V Araon* crews and onboard helicopter pilots without whose service this work would not have been possible. They would also like to thank the German Aerospace Center (DLR) for providing the TerraSAR-X image via the TSX project OCE0644 to B. Hwang.

REFERENCES

- F. Fetterer and N. Untersteiner, "Observations of melt ponds on Arctic sea ice," *J. Geophys. Res.*, vol. 103, no. C11, pp. 24 821–24 835, 1998.
- D. K. Perovich, "The optical properties of sea ice," DTIC Document, 1996.
- J. Ehn, C. J. Mundy, D. G. Barber, H. Hop, A. Rossnagel, and J. Stewart, "Impact of horizontal spreading on light propagation in melt pond covered seasonal sea ice in the Canadian Arctic," *J. Geophys. Res.*, vol. 116, 2011, DOI: 10.1029/2010JC006908C00G02.
- E. L. Andreas, T. W. Horst, A. A. Grachev, P. O. G. Persson, C. W. Fairall, P. S. Guest, and R. E. Jordan, "Parameterizing turbulent exchange over summer sea ice and the marginal ice zone," *Quart. J. Roy. Meteorol. Soc.*, vol. 136, 2010, DOI: 10.1002/qj.618.
- D. Flocco, D. Feltham, and A. Turner, "Incorporation of a physically based melt pond scheme into the sea ice component of a climate model," *J. Geophys. Res.*, vol. 115, no. C8, pp. 1–14, 2010.
- C. A. Pedersen, E. Roeckner, M. Juthje, and J.-G. Winther, "A new sea ice albedo scheme including melt ponds for ECHAM5 general circulation model," *J. Geophys. Res.*, vol. 114, 2011, DOI: 10.1029/2008JD010440D08101.
- J. Hanesiak, J. J. Yackel, and D. G. Barber, "Effect of melt ponds on first-year sea ice ablation—Integration of RADARSAT-1 and thermodynamic modelling," *Can. J. Remote Sens.*, vol. 27, no. 5, pp. 433–442, 2001.
- J. Curry, J. Schramm, and E. Ebert, "Sea ice-albedo climate feedback mechanism," *J. Climate*, vol. 8, no. 2, pp. 240–247, 1995.
- L. Rabenstein, S. Hendricks, T. Martin, A. Pfaffhuber, and C. Haas, "Thickness and surface-properties of different sea-ice regimes within the arctic trans polar drift: Data from summers 2001, 2004 and 2007," *J. Geophys. Res.*, vol. 115, 2010, DOI: 10.1029/2009JC005846C12059.
- P. Sankelo, J. Haapala, I. Heiler, and E. Rinne, "Melt pond formation and temporal evolution at the drifting station Tara during summer 2007," *Polar Res.*, vol. 29, no. 3, pp. 311–321, 2010.
- M. A. Tschudi, J. Curry, and J. Maslanik, "Airborne observations of summertime surface features and their effect on surface albedo during FIRE/SHEBA," *J. Geophys. Res.*, vol. 106, no. D14, pp. 15 335–15 344, 2001.
- A. Roesel and L. Kaleschke, "Comparison of different retrieval techniques for melt ponds on Arctic sea ice from Landsat and MODIS satellite data," *Ann. Glaciol.*, vol. 52, no. 57, pp. 185–191, 2011.
- M. A. Tschudi, J. A. Maslanik, and D. K. Perovich, "Derivation of melt pond coverage on Arctic sea ice using MODIS observations," *Remote Sens. Environ.*, vol. 112, no. 5, pp. 2605–2614, 2008.
- F. Fetterer, S. Wilds, and J. Sloan, "Arctic sea ice melt pond statistics and map, 1999–2001," National Snow and Ice Data Center, Digital Media, Boulder, CO, 2008.
- P. Lu, Z. Li, B. Cheng, R. Lei, and R. Zhang, "Sea ice surface features in Arctic summer 2008: Aerial observations," *Remote Sens. Environ.*, vol. 114, no. 4, pp. 693–699, 2010.
- A. J. Schweiger, "Changes in seasonal cloud cover over the Arctic seas from satellite and surface observations," *Geophys. Res. Lett.*, vol. 31, no. 12, 2004, L12207.
- R. K. Scharien, J. J. Yackel, M. A. Granskog, and B. G. T. Else, "Coincident high resolution optical-SAR image analysis for surface albedo estimation of first-year sea ice during summer melt," *Remote Sens. Environ.*, vol. 111, no. 2–3, pp. 160–171, 2007.
- J. Yackel, D. Barber, and T. Papakyriakou, "On the estimation of spring melt in the North Water Polynya using RADARSAT-1," *Atmosphere-Ocean*, vol. 39, no. 3, pp. 195–208, 2001.
- S. Gantert, G. Riegler, F. Teufel, O. Lang, L. Petrat, W. Koppe, and J. Herrmann, "TerraSAR-X, TanDEM-X, TerraSAR-X2 and their applications," in *Proc. 3rd Int. Asia-Pacific Conf. Synthetic Aperture Radar*, Seoul, Korea, 2011, pp. 1–4.
- D. K. Perovich, K. F. Jones, B. Light, H. Eicken, T. Markus, J. Stroeve, and R. Lindsay, "Solar partitioning in a changing Arctic sea-ice cover," *Ann. Glaciol.*, vol. 52, pp. 192–196, 2011.
- B. J. Hwang, A. Langlois, D. G. Barber, and T. N. Papakyriakou, "On detection of the thermophysical state of landfast first-year sea ice using *in-situ* microwave emission during spring melt," *Remote Sens. Environ.*, vol. 111, no. 2–3, pp. 148–159, 2007.
- J. Iacozza and D. G. Barber, "Ablation patterns of snow cover over smooth first-year sea ice in the Canadian Arctic," *Hydrol. Processes*, vol. 15, no. 18, pp. 3559–3569, 2001.
- H. Eicken, H. R. Krouse, D. Kadko, and D. K. Perovich, "Tracer studies of pathways and rates of meltwater transport through Arctic summer sea ice," *J. Geophys. Res.*, vol. 107, no. C10, 2002, DOI:10.1029/2000JC000583.
- D. K. Perovich, W. B. Tucker, III, and K. A. Ligett, "Aerial observations of the evolution of ice surface conditions during summer," *J. Geophys. Res.*, vol. 107, no. C10, 2002, DOI: 10.1029/2000JC000449.
- J. Yackel, D. Barber, and J. Hanesiak, "Melt ponds on sea ice in the Canadian Archipelago 1. Variability in morphological and radiative properties," *J. Geophys. Res.*, vol. 105, no. C9, pp. 22 049–22 060, 2000.
- J. Yackel and D. Barber, "Melt ponds on sea ice in the Canadian Archipelago 2. On the use of RADARSAT-1 synthetic aperture radar for geophysical inversion," *J. Geophys. Res.*, vol. 105, no. C9, pp. 22 061–22 070, 2000.
- M. A. Tschudi, J. A. Curry, and J. Maslanik, "Determination of areal surface-feature coverage in the Beaufort Sea using aircraft video data," *Ann. Glaciol.*, vol. 25, pp. 434–438, 1997.
- T. Markus, D. J. Cavalieri, and A. Ivanoff, "The potential of using Landsat 7 ETM+ for the classification of sea-ice surface conditions during summer," *Ann. Glaciol.*, vol. 34, no. 1, pp. 415–419, 2002.
- T. Markus, D. J. Cavalieri, and M. A. Tschudi, "Comparison of aerial video and Landsat 7 data over ponded sea ice," *Remote Sens. Environ.*, vol. 86, no. 4, pp. 458–469, 2003.
- R. G. Barry, "The parameterization of surface albedo for sea ice and its snow cover," *Progr. Phys. Geography*, vol. 20, no. 1, pp. 63–79, 1996.
- D. J. Robinson, N. J. Redding, and D. J. Crisp, "Implementation of a fast algorithm for segmenting SAR imagery," DTIC Document, 2002.

ABOUT THE AUTHORS

Duk-jin Kim (Member, IEEE) received the B.Sc. degree in Earth system science and the M.Sc. and Ph.D. degrees in radar remote sensing and geophysics from Seoul National University, Seoul, Korea, in 1999, 2001, and 2005, respectively.

From October 2005 to July 2007, he was a Postdoctoral Researcher with the University of Manitoba, Winnipeg, MB, Canada, and with the University of Michigan, Ann Arbor. From July 2007 to August 2008, he was a Senior Researcher with the Remote Sensing Division, Korea Aerospace Research Institute (KARI), Daejeon, Korea. He is currently an Associate Professor in the School of Earth and Environmental Sciences, Seoul National University. His research interests include natural disaster monitoring, ocean/sea ice parameter extraction, coastal environment monitoring, and algorithm development, using various SAR systems, including cross-track and along-track interferometric SAR, polarimetric SAR, as well as conventional SAR systems.

Prof. Kim is a member of the American Geophysical Union (AGU) and the Korean Society of Remote Sensing (KSRS).



Hyung-Sup Jung (Member, IEEE) received the M.S. and Ph.D. degrees in geophysics and remote sensing from Yonsei University, Seoul, Korea, in 1998 and 2007, respectively.

He is currently an Assistant Professor with the Department of Geoinformatics, University of Seoul, Seoul, Korea. His primary research interests include developments of synthetic aperture radar (SAR), interferometric SAR (InSAR), multiple-aperture InSAR (MAI), and small baseline subset (SBAS) InSAR processors, and algorithms related to 3-D deformation mapping by combining MAI and InSAR and 2-D surface velocity estimation by combining MAI and along-track interferometry.



Byongjun Hwang received the B.S. and M.S. degrees in marine science from Hanyang University, Ansan, Korea, in 1991 and 1997, respectively, and the Ph.D. degree from the University of Manitoba, Winnipeg, MB, Canada, in 2008.

He has been involved in research on *in situ* microwave radiometer and scatterometer measurements and the application of microwave remote sensing of sea ice. He has participated in international Arctic field experiments involving scatterometer and radiometer measurements. He is currently a Sea Ice Physicist and Remote Sensing Specialist at the Scottish Association for Marine Science, Oban, Argyll, U.K., where his research interests include high-resolution synthetic aperture radar application in sea ice study, sea ice drift, and sea ice mass balance.



Wooil M. Moon (Fellow, IEEE) received the B.A.Sc. degree in electrical engineering from the University of Toronto, Toronto, ON, Canada, in 1970, the M.Sc. degree in geophysics from Columbia University, New York, NY, in 1972, and the Ph.D. degree in geophysics from the University of British Columbia, Vancouver, BC, Canada, in 1976.

In 1979, he joined the Faculty of Science, University of Manitoba, Winnipeg, MB, Canada, where he is now a Professor Emeritus in Residence (Geophysics). He was invited by Seoul National University, Seoul, Korea, in 1998, where he supervised graduate students. He has participated and has worked as a principal investigator (PI) for numerous application development and science verification projects including SEASAT, JERS-1, RADARSAT-1, NASA(JPL) AIRSAR, ERS-1/2, ENVISAT, ALOS, TerraSAR-X, and RADARSAT-2. His research interests include radar altimetry, synthetic aperture radar (SAR), polarimetric SAR theory and applications, and spatial data fusion and spatial reasoning.



Dr. Moon is a member of the American Geophysical Union (AGU), the Canadian Geophysical Union (CGU), the American Institute of Physics (AIP), the Canadian Aeronautics and Space Institute (CASI), the Canadian Association of Physicists (CAP), the Geological Society of Korea, and the Society of Exploration Geophysicists (SEG). He has been a Council member of the International Union of Geodesy and Geophysics (IUGG) since 2004. He is also an elected Founding Member of CGU and a Fellow of the Korean Academy of Science and Technology (KAST).

Kyung Ho Chung, photograph and biography not available at the time of publication.

Sang Hoon Lee, photograph and biography not available at the time of publication.